MDPI

Article

Numerical Investigation of Thermally Developing and Fully Developed Electro-Osmotic Flow in Channels with Rounded Corners

Nicola Suzzi [1],[†] and Marco Lorenzini [2],[*],[†]

1   Dipartimento Politecnico di Ingegneria e Architettura, Università degli Studi di Udine, Via delle Scienze 206, 33100 Udine, Italy; nicola.suzzi@uniud.it
2   Dipartimento di Ingegneria Industriale, Campus di Forlì, Università di Bologna, Via Fontanelle 40, 47131 Forlì, Italy
*   Correspondence: marco.lorenzini@unibo.it
†   These authors contributed equally to this work.

Abstract: Electro-osmotic flow, that is, the motion of a polar fluid in microducts induced by an external electric field, is one micro-effect which allows fluid circulation without the use of mechanical pumping. This is of interest in the thermal management of electronic devices, as microchannels with cross sections of almost arbitrary shape can easily be integrated on the chips. It is therefore important to assess how the geometry of the channel influences the heat transfer performance. In this paper, the thermal entry region and the fully developed electro-osmotic flow in a microchannel of rectangular cross section with smoothed corners is investigated for uniform wall temperature. For the fully developed region, correlations for the Poiseuille and Nusselt numbers considering the aspect ratio and nondimensional smoothing radius are given, which can be used for practical design purposes. For thermally developing flow, it is highlighted how smoothing the corners increases the value of the local Nusselt number, with increases up to 18% over sharp corners, but that it also shortens the thermal entry length. It is also found that Joule heating in the fluid may cause a reversal of the heat flux, and that the thermal entry length has a linear dependence on the Reynolds number and the hydraulic diameter and on the logarithm of the nondimensional Joule heating.

Keywords: electro-osmosis; microchannel; thermal entry length; convective heat transfer; laminar flow

1. Introduction

Fundamental research on microchannels has given rise to a vast body of studies ever since the seminal work by Tuckerman and Pease almost four decades ago [1]. Knowledge acquired over the years allowed microchannels to establish themselves as the building blocks of so-called micro-flow devices (MFDs), as can be realized by comparing older reviews on the subject [2,3], to more recent ones [4–6], a fact also recognized by the Tuckerman and Pease themselves in a retrospective article published in 2012 [7].

Currently, there is still an amount of research addressing fundamental subjects [8–16], but MFDs have now found applications in several fields [17], e.g., micro heat exchangers (MHXs) are employed in air conditioning systems [18] and heat pumping equipment [19]. The use of microjets and two-phase flow as cooling means has been investigated and applied too [20–22]. Microchannel heat sinks, a subset of MHXs, have great applicative potential where removal of high heat fluxes is in demand. This makes them particularly interesting for the thermal management of electronic devices, which are steadily growing in compactness and, as a consequence, in power density. Pressure drop across such devices, however, may be significant, especially when liquids are employed as coolants, with the reduction in hydraulic diameter of the ducts quickly leading to viscous heating of the fluid circulated [23] which reverses the direction of the heat flow.

At small scales, however, flow devices can exploit micro-effects such as electro-osmosis, which allows the motion of a liquid relative to a charged surface, induced by an applied external potential gradient across a microchannel [24,25]. If a polar fluid is used in combination with channel walls possessing a net electrical charge, an inhomogeneous charge distribution develops in the liquid, which can be moved by applying electric field over the length of the channel, which acts on the layer of mobile ions close to the walls: the flow which originates is called electro-osmotic (EOF). EOF devices have several advantages: they do not have moving parts, are therefore free of noise and vibrations and no lubrication is needed. Furthermore, liquid reservoirs require tiny volumes, making them ideal for direct connection to the chips. EOFs have been reported to yield experimental Nusselt numbers about 10% larger than pressure-driven flow (PDF) for the same geometry, although Joule heating may become significant when applied voltage between the electrodes increases beyond a certain threshold [26]. Voltage signals sent to electrodes make implementation of EOF devices easier than manufacturing and controlling a micro mechanical pump. Among the drawbacks, the chemical composition at the interface can significantly alter the velocity profiles, which are markedly different from those exhibited by pressure-driven flows, and Joule heating in the fluid may partly or completely offset its cooling action [24]. Electro-osmotic flows in microchannels have been the subject of several fundamental investigations, for a variety of cross sections, ranging from the common circular ducts and parallel plates [27,28], to unusual geometries such as polygonal, elliptical and triangular ducts [29–31], as has been the use of electro-osmotic pumps (EOPs) [26,32,33], sometimes with the specific purpose of electronics cooling [26,34,35]. The use of non-Newtonian fluids [36,37] and nanofluids [38] is also a recent field of investigation.

The brief overview above reveals how research on electro-osmotic flow in microchannels has been very active in the recent past, touching on a variety of subjects such as the fluids employed, the electric field magnitude, the presence of the pressure gradient, and the shape of cross section, which can take several forms (circular, trapezoidal, rectangular, etc.) thanks to the current development of micro-fabrication technologies. Optimization of the cross section can lead to improved performance in terms of increased heat transfer and decreased pressure drop and entropy production, and this can be achieved through smoothing of its corners, as demonstrated in [39,40]. Investigation has been extended to pressure-driven flows in microchannels with and without viscous dissipation [41–43], and to electro-osmotic flows in the fully developed and constant heat flux and perimeter temperature case [44,45], employing the results to carry out a first-law analysis based on performance evaluation criteria (PEC) [46].

To the best of the Authors' knowledge, no attempt has been made so far to analyze EOFs in the thermal entry region (the so-called Graetz problem) of a microchannel of rectangular cross section with smoothed corners; therefore, this work aims at filling this gap for the case of uniform temperature of the channel walls, so-called T boundary condition [47]. The fully developed case is also studied in order to provide correlations of practical use for the Poiseuille and Nusselt numbers as a function of both the aspect ratio β and the nondimensional radius of curvature, γ.

The influence of β and γ on the nondimensional thermal entry length is also investigated, as is the dependence of the latter on quantities such as Joule heating, hydraulic diameter, and Reynolds and Peclet numbers. The aim is both to deepen the fundamental understanding of the phenomenon and to gain insights of practical applicability to such devices as heat sinks and micropumps.

The results are also useful for the purpose of conducting optimization studies, e.g., using PEC-type approaches.

2. Mathematical Model

This section reports the nondimensional forms of the governing equations for the electric potential, velocity, and temperature fields and the boundary conditions which are used to solve the problem; the dimensional forms and the normalizing quantities used

to obtain them are reported in Appendix A. The equations are written for a Cartesian coordinate system, which has x as the axial coordinate (flow direction), while y and z are the coordinates of the cross section (orthogonal to flow direction), as illustrated in Figure 1.
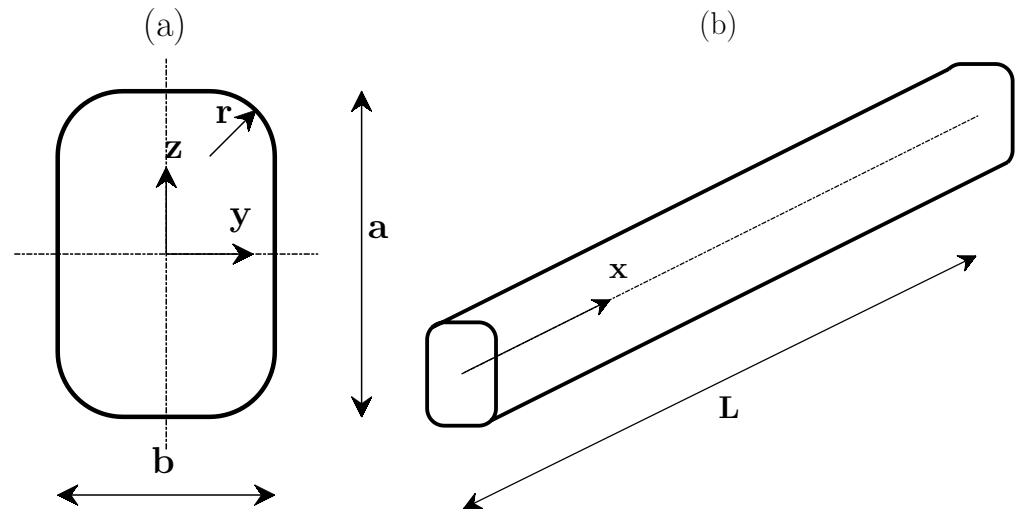

Figure 1. Channel cross section geometry (**a**), channel axis (**b**), and reference Cartesian coordinate system (**a**,**b**).

2.1. Electric Potential Field

The nondimensional formulation of the equation governing the electric potential distribution is shown below,

$$\frac{\partial^2 \Psi}{\partial Y^2} + \frac{\partial^2 \Psi}{\partial Z^2} = (k_D \, D_h)^2 \, \sinh \Psi \tag{1}$$

where k_D is the Debye–Hückel parameter (m^{-1}):

$$k_D = \sqrt{\frac{2 \, e^2 \, c_0 \, z_i^2}{\epsilon \, k_B \, T}} \tag{2}$$

The value of the potential at the Stern plane ζ is used as a boundary condition over the channel wall:

$$\Psi|_{\partial \Omega} = \frac{z_i \, e}{k_B \, T} \, \zeta = \Psi_0 \tag{3}$$

As T-boundary conditions are applied to the temperature field, the nondimensional electric potential Ψ, the Debye–Hückel parameter k_D, and the nondimensional Stern potential Ψ_0, Equations (2) and (3) are defined with respect to the imposed wall temperature T_w, which is chosen as the characteristic temperature. Accordingly, variations of T_w and, subsequently, of the inlet temperature of the fluid, T_i, when the temperature drop $T_w - T_i$ is fixed, determine the range of values taken by the Debye–Hückel parameter in this work.

2.2. Velocity Field

A steady, hydrodynamically developed laminar flow of a Newtonian, incompressible fluid with uniform thermophysical properties through a microchannel of uniform cross section with rigid, non-porous wall is considered.

Starting from the governing equation and introducing suitable normalising quantities, as reported in Appendix A.2, the component along x axis of Equation (A5) can be written in nondimensional form:

$$\frac{\partial^2 U}{\partial Y^2} + \frac{\partial^2 U}{\partial Z^2} = \tilde{E} \, \sinh \Psi \tag{4}$$

The no-slip boundary condition is imposed through the solid wall, $U|_{\partial\Omega} = 0$. The only velocity component in the case of fully-developed flow is along the X direction; therefore, equations for the other two velocity components are not shown.

Once the velocity field $U(Y, Z)$ is computed, the corresponding Poiseuille number can be estimated, details are given in Appendix A.2.

2.3. Temperature Field

The nondimensional temperature distribution $\Theta(X, Y, Z)$ is obtained from the solution of the nondimensional energy equation below,

$$\mathrm{Re\,Pr}\,\frac{U}{U_b}\frac{\partial\Theta}{\partial X} = \frac{\partial^2\Theta}{\partial Y^2} + \frac{\partial^2\Theta}{\partial Z^2} + Q \tag{5}$$

where Pr is the Prandtl number of the fluid, while U_b and Re are the nondimensional bulk velocity and the Reynolds number,

$$\mathrm{Re} = \frac{\rho\,u_b\,D_h}{\mu} \tag{6}$$

with $u_b = u_0\,U_b$ the dimensional bulk velocity.

The temperature T_w is imposed (T-boundary conditions) through the channel wall, and a uniform temperature profile is chosen over the inlet section $X_0 = 0$ of the channel:

$$\Theta|_{\partial\Omega} = 0,\ \Theta(Y,Z)|_{X_0} = 1 \tag{7}$$

The choice of the boundary conditions imposed to the temperature field through the inlet section will be discussed further in Section 3.

Once the temperature field $\Theta(X, Y, Z)$ is computed, the average Nusselt number along channel axis can be estimated, as explained in Appendix A.3.

3. Materials and Methods

3.1. Numerical Modeling

The numerical solution of the governing equations—Equations (1), (4) and (5)—was obtained using the open source software `GNU Octave`. Additional libraries, provided by `Octave Forge`, were used: the `msh` package, which relies on the open source software `gmsh`, allows to generate triangular and tetrahedral unstructured meshes for Finite Element Method (FEM) or Finite Volume Method (FVM) solvers, and the `bim` package, which implements both the Finite Volume Scharfetter–Gummel (FVSG) method and the Finite Element Method (FEM), allows to solve Diffusion Advection Reaction (DAV) partial differential equations. The functions `bim2a_laplacian`, `bim2a_reaction`, and `bim2a_rhs` belonging to `bim` library allow to assemble the finite element discretised operators for solving partial differential equations of the form

$$-\nabla\cdot(C_1\nabla\phi) + C_2\phi = C_3 \tag{8}$$

on a two-dimensional (2D) unstructured, triangular mesh.

The 2D computational domain, consisting of the channel cross section geometry, is discretized through `gmsh` software, using a triangular mesh with increased accuracy imposed close to the cross section perimeter, where higher gradients for both the electric potential and the velocity fields are expected. Equation (1) is numerically solved first over the 2D mesh of the channel cross section to compute the electric potential $\Psi(Y, Z)$. In order to reduce Equation (1) to the same form of Equation (8), linearization of the reaction term, $(k_D\,D_h)^2\sinh\Psi$, is carried out using a first-order Taylor polynomial and the numerical solution of Equation (1) is iterated until convergence of the electric potential field is obtained. Then, the numerical solution of Equation (4), which requires the knowledge

of Ψ, is computed and the developed velocity field $U(Y, Z)$ is solved over the channel cross section.

As the energy equation, Equation (5), has the form of a parabolic partial differential equation, the three-dimensional physical problem can be reduced to a 2D mathematical problem. Implementing the $\theta-$weighted scheme for marching over channel axis, Equation (5) is discretized as

$$\mathrm{Re}\,\mathrm{Pr}\,\frac{U}{U_b}\left[\frac{\Theta}{\Delta X}\right]^{n+1} - \theta\left[\frac{\partial^2\Theta}{\partial Y^2} + \frac{\partial^2\Theta}{\partial Z^2}\right]^{n+1} = \mathrm{Re}\,\mathrm{Pr}\,\frac{U}{U_b}\left[\frac{\Theta}{\Delta X}\right]^{n} + (1-\theta)\left[\frac{\partial^2\Theta}{\partial Y^2} + \frac{\partial^2\Theta}{\partial Z^2}\right]^{n} + Q \tag{9}$$

where n denotes the integration step along the channel axis. At each step n, Equation (9), which has the same form as Equation (8), is numerically solved over the 2D mesh of the channel cross section through `bim` library functions.

3.2. Problem Setup

The electro-osmotic flow over a channel of length L with constant cross section is investigated. The geometrical configuration, defined by a rectangular cross section with rounded corners as shown in Figure 1, is characterized by the aspect ratio $\beta = b/a \in [0,1]$ and the nondimensional smoothing radius $\gamma = 2\,r/b \in [0,1]$. The corresponding hydraulic diameter can be calculated as a function of the length of the longer side, a, and of the nondimensional parameters β and γ:

$$D_h = 2\,a\,\frac{\beta - (\beta\,\gamma)^2(4-\pi)}{(1+\beta) - (\beta\,\gamma)(4-\pi)} \tag{10}$$

Taking advantage of the problem symmetry, only one-quarter of the whole channel section is investigated, in order to reduce the computational cost of simulations, and symmetry conditions are imposed through the lines $Y = 0$ and $Z = 0$,

$$\nabla\Psi \cdot \hat{\mathbf{n}} = 0,\ \nabla U \cdot \hat{\mathbf{n}} = 0,\ \nabla\Theta \cdot \hat{\mathbf{n}} = 0 \tag{11}$$

Dirichlet boundary conditions are imposed along the heated perimeter Γ,

$$\Psi|_{\Gamma} = \frac{z_i\,e}{k_B\,T_w} = \Psi_0,\ U|_{\Gamma} = 0,\ \Theta|_{\Gamma} = 0 \tag{12}$$

which correspond to imposed Stern potential, no-slip condition, and prescribed wall temperature respectively. In addition, an inlet temperature profile must be imposed in order to solve the energy equation, Equation (5). As pointed out in [48,49], when a heat source is present, an adiabatic preparation of the fluid (at least over the hydrodynamically developing region) should be provided in order to ensure physical consistency of the boundary conditions at $X = 0$. Yet, under certain flow conditions the increase in the bulk temperature ΔT_0 due to Joule heating over the adiabatic section can be neglected if compared to the prescribed temperature difference between wall and inlet. This makes the uniform inlet temperature profile a still consistent approximation. In fact, writing the macroscopic energy balance over the adiabatic section,

$$\Delta T_0 = \frac{q'''\,D_h{}^2}{\lambda}\,\frac{L_0}{D_h}\,(\mathrm{Re}\,\mathrm{Pr})^{-1} \tag{13}$$

and assuming that L_0 equals the hydrodynamically developing length, $L_{hy} = 0.05\,\mathrm{Re}\,D_h$, the increment ΔT_0 reduces to

$$\Delta T_0 = \frac{1}{20}\,\frac{q'''\,D_h{}^2}{\lambda}\,\mathrm{Pr}^{-1} \Rightarrow \Delta\Theta_0 = \frac{Q}{20\,\mathrm{Pr}} \tag{14}$$

If water at ambient temperature $T_{amb} = 20\,°C$ is considered, i.e., $Pr \approx 7$, $\Delta\Theta_0 < 7.2\%$ is ensured for $Q \leq 10$, which corresponds to the maximum value of the heat source investigated in this paper.

The Graetz problem for an electro-osmotic flow, which consists of the numerical solution of Equations (1), (4) and (5) with the prescribed boundary conditions, is defined by the following parameters:

- aspect ratio β of the channel cross section;
- nondimensional smoothing radius γ;
- nondimensional Stern potential Ψ_0;
- nondimensional parameter $k_D D_h$, defined by Equation (2), which affects the electric potential field;
- nondimensional electric field $\tilde{E} = E D_h / \zeta$, which causes fluid motion;
- nondimensional heat source Q due to Joule heating; and
- reference Peclet number,

$$\mathrm{Pe} = \left(\rho\, u_0\, c_p\right)\left(D_h\, \lambda^{-1}\right) = 2\,\mathrm{Pr}\,\frac{\rho\, c_0\, e\, \zeta\, D_h{}^2}{\mu^2} \tag{15}$$

where u_0 is the reference velocity, calculated through Equation (A6).

Note that the reference Peclet number is not fully representative of the flow characteristics. The effective value of the Peclet number,

$$\mathrm{Pe} = \left(\rho\, u_b\, c_p\right)\left(L_{th}\, \lambda^{-1}\right) \tag{16}$$

is verified a posteriori to vary in the range $2 \times 10^1 < \mathrm{Pe} < 4 \times 10^2$; this makes the assumption of negligible axial conduction a consistent approximation.

3.3. Grid Independence Analysis

A grid independence analysis (GDA) was also conducted before running several parametric computations. Excluding simulations involving model verification and comparison with literature results, the values of the Debye–Hückel parameter and the nondimensional Stern potential were set to $k_D D_h \leq 9.77$ and $\Psi_0 \leq 3.89$ respectively for most of the parametric computations. As mentioned at the end of Section 2.1, these are determined by the choice of the wall and fluid inlet temperatures; the remaining quantities which compose the Debye–Hückel parameter and the Stern potential have the values of deionized, ultra-filtered water, and are often adopted in the literature [28,30–33,44,45,50]. The highest values were considered for the GDA, while the channel cross section aspect ratio and the smoothing radius were set to $\beta = 3/4$ and $\gamma = 1/2$.

Equations (3), (4) and (A15) were numerically solved for increasing mesh accuracy, which is defined by the imposed grid spacing parameter l_c. Both the Poiseuille and Nusselt numbers of the fully developed flow were computed through Equations (A7) and (A14). Results are listed in Table 1, where the corresponding numbers of mesh nodes and triangular elements are also reported, and are plotted in Figure 2. As a discrepancy of less than 0.35‰ was observed for Po reducing l_c from 5×10^{-3} to 2.5×10^{-3}, a value of $l_c = 5 \times 10^{-3}$ was chosen for all the numerical computations. Figure 2 also shows the triangular mesh, generated through the `gmsh` software, for $l_c = 4 \times 10^{-2}$: it can be noticed that mesh refinement occurs along the heated perimeter, where higher gradients of the electric potential $\Psi(Y,Z)$, velocity $U(Y,Z)$ and developed temperature $\Theta_\infty(Y,Z)$ fields are expected.

When the Graetz problem is solved, the discretization step ΔX over the channel axis direction is imposed in order to ensure at least 200 iterations before thermally developed condition is reached,

$$L_{th}\;:\;\left|1 - \frac{\mathrm{Nu}(L_{th})}{\mathrm{Nu}_\infty}\right| \leq 0.05 \tag{17}$$

where $\mathrm{Nu}(X)$ and Nu_∞ are computed via Equations (A12) and (A14).

Table 1. Computed Poiseuille number and Nusselt number for different values of mesh accuracy, number of nodes N_p, and number of triangular elements N_t. $\beta = 3/4$, $\gamma = 1/2$, $k_D D_h = 9.77$, $\Psi_0 = 3.89$.

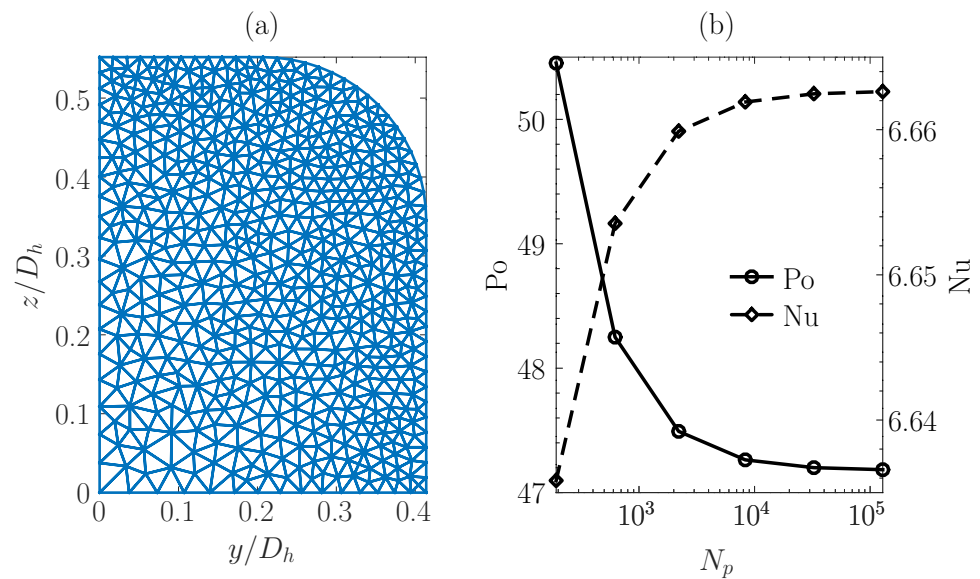| l_c	N_p	N_t	**Po**	**Nu**
8×10^{-2}	192	338	50.4520	6.635831
4×10^{-2}	621	1157	48.2496	6.653541
2×10^{-2}	2205	4248	47.4922	6.659893
1×10^{-2}	8309	16303	47.2633	6.661907
5×10^{-3}	32598	64571	47.2007	6.662473
2.5×10^{-3}	128655	256067	47.1843	6.662622

Figure 2. Triangular mesh for $l_c = 4 \times 10^{-2}$ (**a**). Computed Poiseuille number and Nusselt number for increasing mesh accuracy (**b**). $\beta = 3/4$, $\gamma = 1/2$, $k_D D_h = 9.77$, $\Psi_0 = 3.89$.

4. Results and Discussion

4.1. Model Validation

Comparison with numerical results in the literature was first conducted in order to check the numerical solution of both the Poisson–Boltzmann equation and the momentum equation, Equations (1) and (4), which were both numerically solved in [45] by means of COMSOL Multiphysics®. Considering the same test case as in [45], $k_D D_h = 9.85$ and $\Psi_0 = 7.92$, several geometrical configurations were simulated and the corresponding Poiseuille number computed. As high gradients $\nabla \Psi \cdot \hat{\mathbf{n}}$, due to the high Stern potential, were expected close to the channel wall, the grid spacing parameter was set to $l_c = 2.5 \times 10^{-3}$, leading to meshes with more than 10^5 nodes. A good agreement with the numerical results of [45] can be observed in Table 2, with differences below 1% on the computed Poiseuille number always obtained.

Table 2. Literature vs. computed values of Poiseuille number for different cross-sectional geometries. $k_D D_h = 9.85$, $\Psi_0 = 7.92$.

β	γ	**Po** [45]	**Po**
1	0	161.78	162.60 (+0.51%)
1/2	0	162.63	163.43 (+0.49%)
1/4	0	164.65	165.25 (+0.36%)
1	1	162.15	163.55 (+0.86%)

The electric potential field was also qualitatively verified with the analytical solution, which is available in the limiting case of a cylindrical duct for Stern potential approaching zero. Solving the axisymmetric Poisson–Boltzmann equation under Debye–Hückel linearization, i.e., $\lim_{\Psi \to 0}(\sinh \Psi) \to \Psi$, gives [51],

$$\Psi(R) = C_1 \, I_0(k_D D_h \, R) + C_2 \, K_0(k_D D_h \, R) \tag{18}$$

where $R \in [0, 1/2]$ is the nondimensional radial coordinate; I_0 and K_0 are the first and second kind of modified Bessel functions; and C_1 and C_2 are constants defined by the boundary conditions imposed.

As a fully developed flow subject to H-boundary condition was investigated in [45], comparison was not possible. However, the developed temperature field under T-boundary condition was quantitatively verified with the analytical solution available for a cylindrical duct. Solving the axisymmetric energy equation for a fully developed flow under T-boundary conditions gives the analytical temperature profile,

$$\Theta(R) = \frac{Q}{4} \left(\frac{1}{4} - R^2 \right) \tag{19}$$

where R is the nondimensional radial coordinate.

Both normalized, numerical electric potential profiles for different values of the imposed Stern potential Ψ_0 and normalized, analytical electric potential, valid in the limit of Ψ_0 approaching zero, are plotted in Figure 3 over the cylindrical cross section: note that the numerical profile approaches the analytical one when low values of Ψ_0 are imposed. The numerical velocity profiles for different values of Ψ_0 are shown in Figure 3: as mentioned, the higher the value of the Stern potential, the higher the velocity gradient close to the channel wall, resulting in a flow pattern similar to plug flow. The developed temperature profile, which is also shown in Figure 3 and does not depend on the velocity profile, was computed both via the numerical solution of Equation (A15) and as the asymptotic behavior for $X \to \infty$ from the solution of Equation (5). Thus, the numerical temperature profile was quantitatively verified with the analytical solution, Equation (19), computing the mean squared error (MSE) at mesh nodes,

$$MSE = \frac{1}{N_p} \sum_{n=1}^{N_p} \left[\Theta_n - \frac{Q}{4} \left(\frac{1}{4} - \sqrt{Y_n{}^2 + Z_n{}^2} \right) \right]^2 = 9.4895 \times 10^{-9}, \ N_p = 109190 \tag{20}$$

showing perfect agreement.

The numerical model was also validated with experimental results from the literature. First, the test case of [52] is replicated. Thus, the bulk flow velocity of an EOF is numerically computed and compared with experimental data of [52], where the Authors used nanoparticle image velocimetry technique to measure the mean EOF velocity over 4.9–24.7 μm thick channels. The physical properties of a dilute aqueous solution of sodium tetraborate (borax) were chosen according to the method in [52]. The ζ potential required for the boundary condition on the potential field is derived from the experimental values of the mobility factor μ_{eo} via the Helmholtz–Smoluchowski formula:

$$\mu_{eo} = \frac{u_b}{E_x} = \frac{\epsilon \, \zeta}{\mu} \tag{21}$$

In Figure 4a, numerical results are compared with the experimental data in [52], showing a good agreement for all the concentrations investigated. A small discrepancy is observed at higher values of the electric field, since a linear relationship between bulk velocity and electric field is predicted by the numerical model. However, a linear relationship was also reported according to [26].
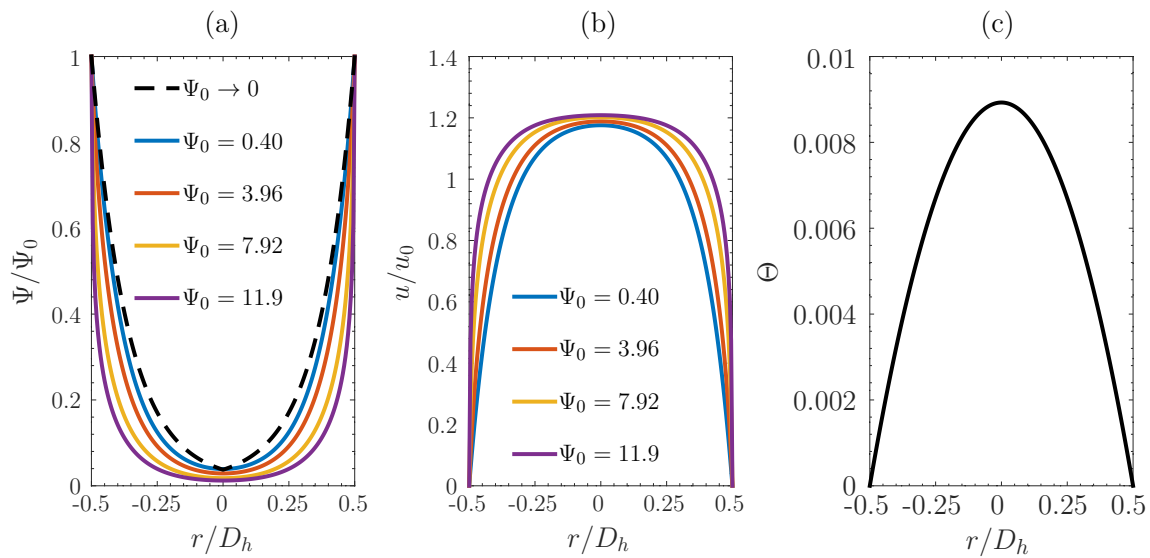
Figure 3. Computed electric potential for different values of the nondimensional Stern potential Ψ_0 and analytical electric potential for Ψ_0 approaching zero (**a**); numerical velocity profile computed for different values of the Ψ_0 (**b**); numerical temperature profile (**c**). $\beta = 1$, $\gamma = 1$, $k_D D_h = 9.77$, $Q = 1.43 \times 10^{-1}$.
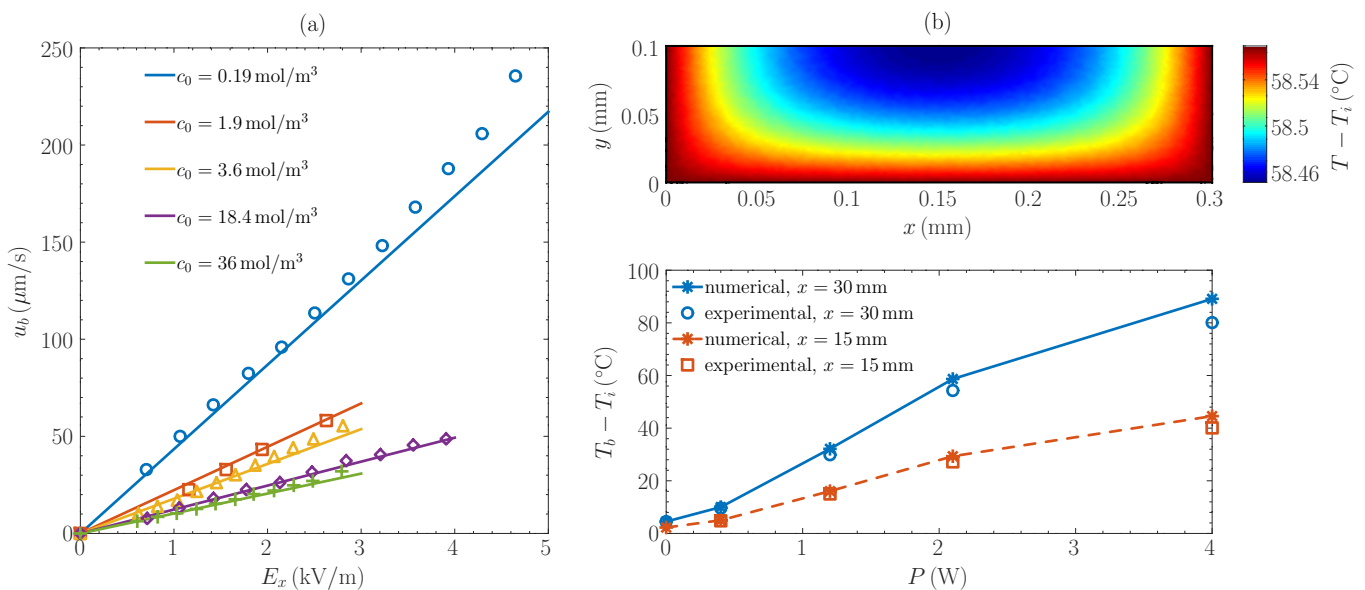

Figure 4. Numerical bulk velocity (continuous line) versus experimental measurements (markers) of [52] for different borax concentrations and imposed electric fields (**a**). Numerical versus experimental [26] bulk temperature as a function of heating power at both the middle section and the outlet section of the microchannel (computed, outlet temperature profile for heating power equal to 2.1 W is also shown) (**b**). Dilute aqueous solution of sodium tetraborate (borax) investigated.

In order to validate the temperature field solution, the experimental setup in [26] was also simulated. In [26], the Authors manufactured and tested a micro-heat sink with the cooling fluid serving both as a heat exchanger and an integrated pump. Twenty parallel $0.3 \times 0.1 \times 30$ mm^3 microchannels were etched on a silicon substrate and covered by a low thermal conductivity PDMS plate. A heater was attached to the bottom. The borax concentration was set to 0.4 mol/m^3, different values of the voltage driving the EOF were imposed and heating powers up to 4 W were investigated in [26]. Equations (1), (4) and (5) were therefore numerically solved and the resulting bulk temperature at both the middle section ($x = 1.5$ cm) and the outlet section ($x = 3$ cm) compared with the experimental data of [26], for different values of the imposed heating power. The required wall potential

was again estimated through Equation (21). Adiabatic conditions were imposed at the channel wall facing the PDMS cover, whilst H1 thermal boundary conditions were applied to the heated perimeter. The required heat flux per unit length was derived from the data supplied in [26]. The electric field was set to 1.33×10^4 V/m. As shown by Figure 4b, numerical temperatures are in good agreement with experimental measurements over the whole heating power range, with a perfect matching observed when the heater is switched off (temperature rise along the channel due solely to Joule heating). The resulting temperature profile through the outlet section is also provided by Figure 4b.

4.2. Fully Developed Flow Solution

After validation, parametric computations were run, in order to investigate the effect of the cross section geometry on the thermal-hydraulic performances of the microchannel. The case of fully developed electro-osmotic flow, defined by Equations (1), (4) and (A15), was first studied. Several values of both the aspect ratio ($\beta = 1/10, 1/5, 3/10, 2/5, 1/2, 3/5, 7/10, 3/4, 4/5, 9/10, 1$) and the smoothing radius ($\gamma = 0, 1/10, 1/5, 3/10, 2/5, 1/2, 3/5, 7/10, 3/4, 4/5, 9/10, 1$) were investigated, while the nondimensional Debye–Hückel parameter was set to $k_D D_h = 9.77$ according to [45,50], and the nondimensional Stern potential to $\Psi_0 = 3.89$, which is roughly half the value analyzed in [45]. Note that the magnitude of both the electric field $\tilde{E}$ and the heat heat source Q do not affect the Poiseuille number and the developed Nusselt number. This is because the velocity and the temperature fields are scaled by changing $k_D D_h$ and $\tilde{E}$, but retain the same shape.

The electric potential field Ψ, the developed velocity field U and the developed temperature field Θ_∞ resulting from a single computation are shown in Figure 5. As pointed out for the cylindrical duct case, significant gradients of both the electric potential and the velocity can be observed close to the cross section wall. The magnitude of both U and Θ linearly depends on the imposed values of $\tilde{E}$ and Q. The local Nusselt number was also numerically estimated as

$$\mathrm{Nu} = -\frac{\nabla \Theta|_\Gamma \cdot \hat{\mathbf{n}}}{\Theta_b} \tag{22}$$

over the heated perimeter of the cross section, Γ. As demonstrated by Figure 6, the highest temperature gradient occurs at the midpoint of the longer side of the rectangular section, whereas smoother slopes are observed close to the rounded corners. Averaging the local Nusselt number along the heated perimeter leads to the mean Nusselt number Nu = 6.662, which can be computed through Equation (A14).
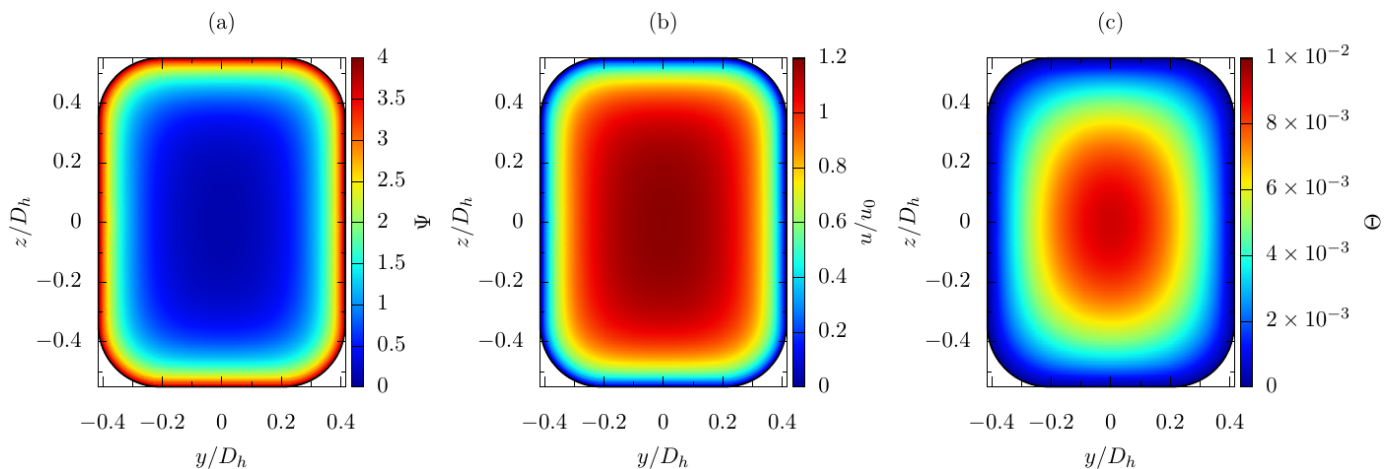

Figure 5. Electric potential field (**a**). Developed velocity field (**b**). Developed temperature field (**c**). $\beta = 3/4$, $\gamma = 1/2$, $k_D D_h = 9.77$, $\Psi_0 = 3.89$, $\tilde{E} = 30$, $Q = 1.43 \times 10^{-1}$.
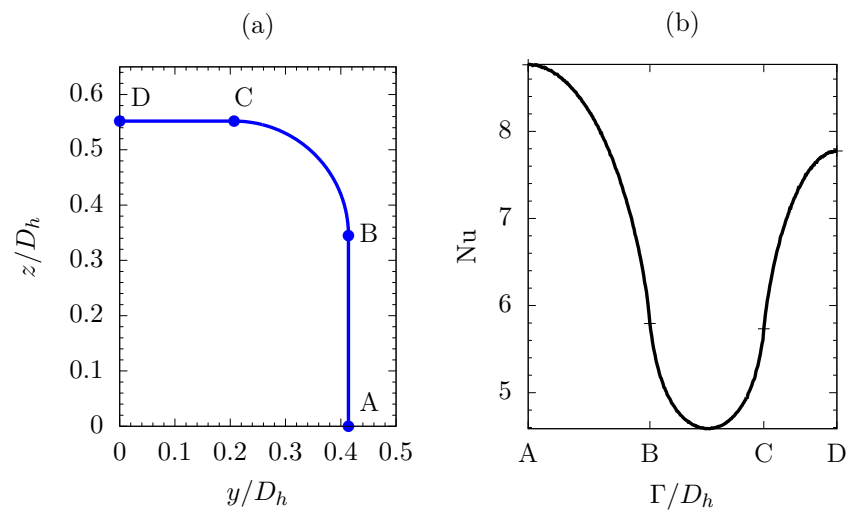
Figure 6. Cross section geometry (**a**). Local Nusselt number of the fully developed flow along the heated perimeter Γ (**b**). $\beta = 3/4$, $\gamma = 1/2$, $k_D D_h = 9.77$, $\Psi_0 = 3.89$.

The results from 110 computations are shown in Figure 7, where the computed Poiseuille and Nusselt numbers are plotted as a function of the channel section geometry, defined by β and γ. The highest values for both Po and Nu were found at $\beta = 1/10$ and $\gamma = 1$, whilst the minimum Po, corresponding to highest efficiency of the micropump, was found for $\beta = 1$ and $\gamma = 0$. Following the approach in [45], the trends of Po and Nu can be approximated, for a given aspect ratio, via a polynomial correlation as a function of the smoothing radius. However, a single, 3rd-order polynomial correlation taking into account the influence of both β and γ is provided here for Po and Nu:

$$\mathrm{Po} = a_{00} + \sum_{n=1}^{3} a_{n0}\, \beta^n + \sum_{n=1}^{3} a_{0n}\, \gamma^n + a_{11}\, a_{11}\, \beta\, \gamma + a_{12}\, \beta\, \gamma^2 + a_{21}\, \beta^2\, \gamma \tag{23}$$

$$\mathrm{Nu} = b_{00} + \sum_{n=1}^{3} b_{n0}\, \beta^n + \sum_{n=1}^{3} b_{0n}\, \gamma^n + b_{11}\, b_{11}\, \beta\, \gamma + b_{12}\, \beta\, \gamma^2 + b_{21}\, \beta^2\, \gamma \tag{24}$$

The corresponding fitting coefficients are listed in Table 3. The Root Mean Square Error, also listed in Table 3, demonstrates that an accurate estimate of both Po and Nu is ensured.
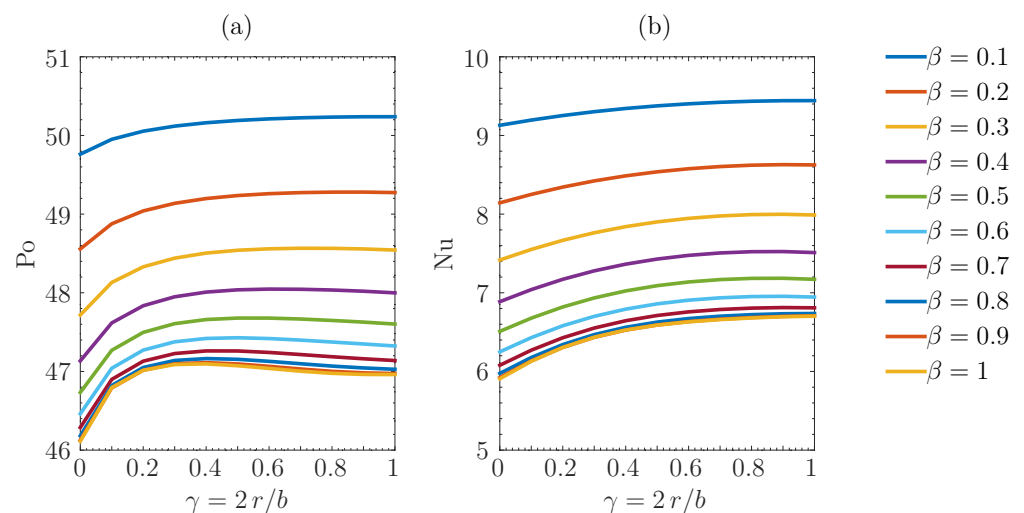

Figure 7. Poiseuille number as a function of the cross-sectional geometry (**a**). Nusselt number as a function of the cross-sectional geometry (**b**). $k_D D_h = 9.77$, $\Psi_0 = 3.89$.

Table 3. Fitting coefficients of Equations (23) and (24) for the estimation of the Nusselt and Poiseuille numbers of a fully developed flow and Root Mean Square Error from 110 numerical points.

Poiseuille Number Equation (23)		Nusselt Number Equation (24)	
a_{00}	+50.8162	b_{00}	+10.1790
a_{10}	−14.0158	b_{10}	−12.4539
a_{20}	+14.6258	b_{20}	+12.3036
a_{30}	−5.19479	b_{30}	−4.11363
a_{01}	+3.59595	b_{01}	+1.03360
a_{02}	−6.58458	b_{02}	−1.25171
a_{03}	+3.66162	b_{03}	+0.500750
a_{11}	+2.01872	b_{11}	+1.87850
a_{12}	−1.29980	b_{12}	−0.751240
a_{21}	−0.761764	b_{21}	−0.672452
RMSE	6.53×10^{-2}	*RMSE*	1.68×10^{-2}

4.3. Graetz Problem Solution

Finally, the Graetz problem, defined by Equations (1), (4) and (5), was solved, in order to determine the thermal entry length under different operating conditions. The aspect ratio was fixed to $\beta = 3/4$ and four different, nondimensional radii of curvature, namely, $\gamma = 0$, 1/4, 1/2, 1 were investigated. The Debye–Hückel parameter and the nondimensional Stern potential were set to $k_D D_h = 8.45$ and $\Psi_0 = 2.92$ respectively. The nondimensional electric field and the reference Peclet number were $\tilde{E} = 3 \times 10^2$ and Pe = 1.15. The effect of changing the heat source due to Joule heating, Q, was investigated: several values ranging between 10^{-3} and 10 were simulated and the influence on the thermal entry length assessed. Note that a variation of the heat source Q at fixed $k_D D_h$, Ψ_0, $\tilde{E}$ and Pe, which are the other model input parameters, can be physically obtained varying the reference temperature difference $T_w - T_i$ and the electric conductivity σ (so that Pe is unaffected).

The resulting temperature profile over the channel sections corresponding to $Y = 0$, $Z = 0$ and $X \in [0, 2]$ is shown in Figure 8 for a computation at very high heat generation ($Q = 8.04$) and low electric field ($\tilde{E} = 2.25 \times 10^{-2}$). Even if the fully developed temperature profile is reached shortly after the channel entrance because of the high value of Q, important considerations can be made:

- close to the entry section, the contribution of Joule heating is still negligible and the heat transfer process is mainly driven by conduction and convection, which is the most profitable operating condition for a microchannel heat sink;
- looking at the mean Nusselt number along the channel axis in Figure 8, a vertical asymptote at $X \simeq 0.535$ is observed, corresponding to the change in sign of the fluid bulk temperature;
- for $X > 0.535$, the heat generation due to Joule heating drives the heat transfer process and the microchannel heat sink is no longer able to dissipate heat from the walls; and
- the thermal entry length L_{th} is reached at $X = 1.37$.

Assessing the existence of a change in the direction of heat transfer is obviously important in practical applications, but knowledge of the extension of the thermal entry length is also useful. In fact, if L_{th} occupies a significant portion of the channel, correlations for the Nusselt number that assume fully developed flow cannot be recommended. Therefore, the rest of the section is devoted to the investigation of L_{th}.
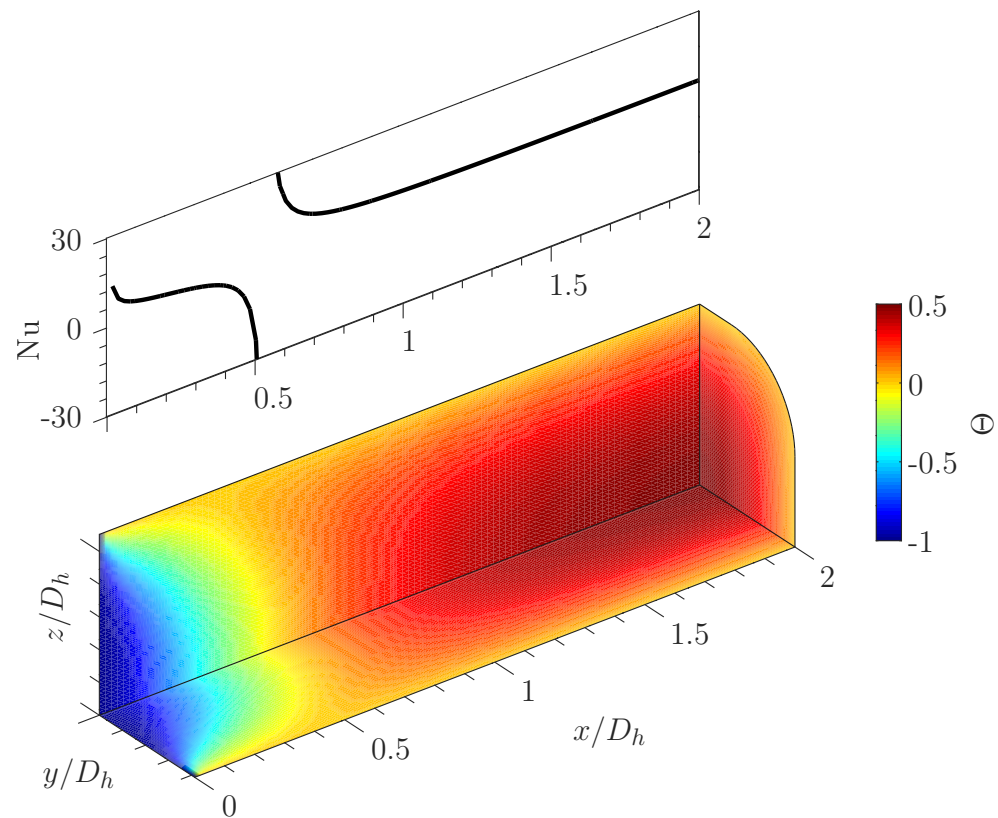
Figure 8. Temperature field over $X = L/D_h$, $Y = 0$, and $Z = 0$ sections of the channel and average Nusselt number along the channel axis. $\beta = 3/4$, $\gamma = 1/2$, $k_D D_h = 9.77$, $\Psi_0 = 3.89$, $\tilde{E} = 2.25 \times 10^2$, $\text{Pe} = 1.15$, $Q = 8.04$.

Results from parametric computations are shown in Figure 9, where the thermal entry length is plotted as a function of the nondimensional source term Q and the smoothing radius γ. It can be pointed out that L_{th} decreases for increasing Joule heating following a logarithmic behavior, when the other model input parameters (namely, $k_D D_h$, Ψ_0, $\tilde{E}$, Pe) are fixed:

$$\frac{L_{th}}{D_h} \propto \log_{10}\left(\frac{1}{Q}\right) \tag{25}$$

The mean Nusselt number along channel axis is also plotted in Figure 9 for different γ and fixed $Q = 1$, showing that

- smoothing the corners shortens the thermal entry length, and, as a consequence, the efficacious channel length (i.e., useful to remove heat from the walls) at high Joule heating, that is for high values of Q;
- heat transfer performance decreases when sharp corners are considered, since lower temperature gradients are observed close to them, meaning that lower Nusselt numbers over the entry region are reached. As an example, in Figure 9 for $x/D_h = 0.9$ Nu goes from 3.95 for $\gamma = 1$ (maximum smoothing) to 3.38 for $\gamma = 0$ (sharp corners);
- small changes in $\text{Nu}(x)$ correspond to significant variations of L_{th} at different values of the smoothing radius γ.

In order to extend the study to a wider range of practical applications, the analysis is expanded to different hydraulic diameters of the channel cross section. Thus, the nondimensional input parameters of the model are scaled with the hydraulic diameter according to their definitions:

$$k_D = \sqrt{\frac{2\,e^2\,c_0\,z_i}{\epsilon\,k_B\,T_w}} \propto D_h{}^0, \; \Psi_0 = \frac{z_i\,e}{k_B\,T_w}\zeta \propto D_h{}^0, \; \tilde{E} = \frac{E_x\,D_h}{\zeta} \propto D_h,$$

$$Q = \frac{\sigma(D_h\,E_x)^2}{\lambda(T_w - T_i)} \propto D_h{}^2, \; \text{Pe} = 2\,\text{Pr}\,\frac{\rho\,c_0\,e\,\zeta\,D_h{}^2}{\mu^2} \propto D_h{}^2 \tag{26}$$

Starting from the set of input parameters investigated and fixing the cross section geometry to $\beta = 3/4$ and $\gamma = 1/2$, computations are run at increasing hydraulic diameters. Thus, beginning at $D_0 = 3\ \mu\text{m}$, the hydraulic diameter is progressively increased up to 15 μm, which corresponds to an increase of the nondimensional Debye–Hückel parameter $k_D\,D_h$ from 8.45 to 42.25. Three different values of the nondimensional heat source, $Q = 10^{-1}$, 10^{-2}, and 10^{-3}, are chosen. Both the thermal entry length and the Reynolds number, the latter resulting from velocity field solution and depending on the imposed hydraulic diameter as well, are computed. Results are plotted in Figure 10.
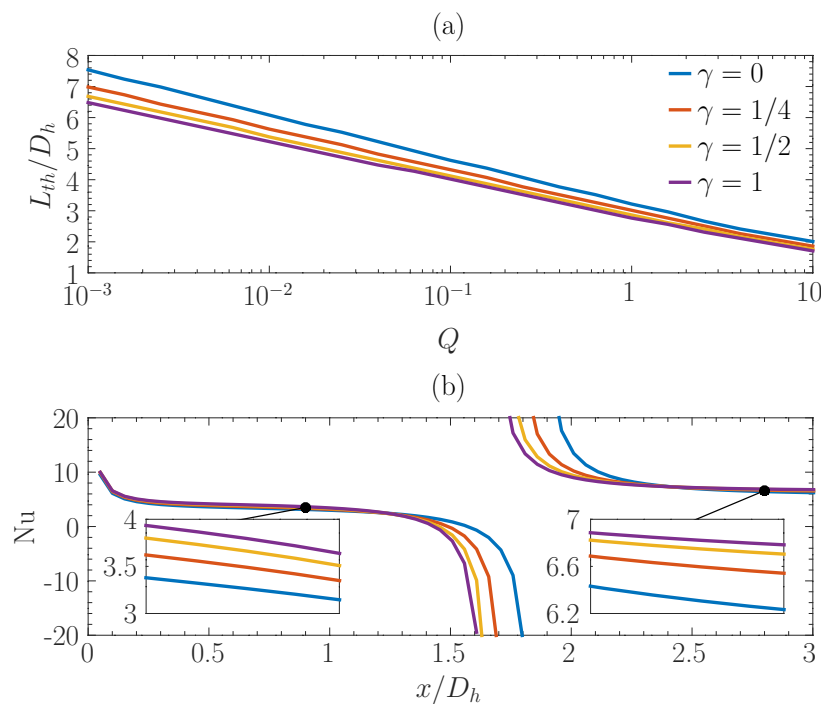

Figure 9. Thermal entry length as a function of nondimensional heat source, due to Joule heating, and smoothing radius (**a**); mean Nusselt number along channel axis for different smoothing radii (legend same as subfigure (**a**) above), $Q = 1$ (**b**). $\beta = 3/4$, $k_D\,D_h = 8.45$, $\Psi_0 = 2.92$, $\tilde{E} = 3 \times 10^2$, $\text{Pe} = 1.15$.

The nondimensional thermal entry length linearly depends on the hydraulic diameter, with values up to $L_{th} = 40\,D_h$ observed when D_h/D_0 approaches 5. This trend can be easily explained looking at Equation (5): the advection term is proportional to Re and Pr, both acting as a scaling parameter for the temperature field evolution along the channel axis, as long as Q is kept constant. On the other hand, this means that L_{th}/D_h weakly depends on the shape of the normalized velocity profile U/U_b, which tends to plug flow for increasing D_h but does not modify the linear correlation between L_{th}/D_h and Re. As discussed earlier for Figure 9, the lower the magnitude of heat source term Q, the longer the nondimensional thermal entry region L_{th}/D_h. The dependence of the Reynolds number on D_h/D_0 is also reported in Figure 10, and is clearly linear. As the magnitude of the dimensional bulk velocity u_b mainly depends on the imposed electric field and the Stern potential but weakly on the hydraulic diameter, as long as $k_D\,D_h \gg 1$, the product of the Prandtl number, which depends on fluid properties, times the Reynolds number $\text{Re} = \rho\,u_b\,D_h/\mu$ is simply proportional to the hydraulic diameter. As a consequence, it can be stated that

the nondimensional length of the thermal entry region L_{th}/D_h linearly depends on the normalized hydraulic diameter D_h/D_0 too.
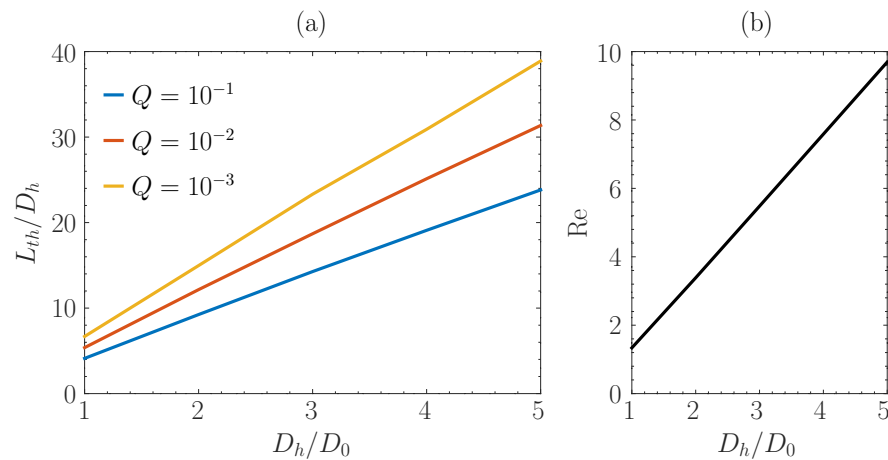

Figure 10. Thermal entry length as a function of the normalized hydraulic diameter (**a**); hydraulic diameter versus Reynolds number (**b**). $\beta = 3/4$, $\gamma = 1/2$, $\Psi_0 = 2.92$, $\tilde{E} \in [3, 12] \times 10^2$, $k_D D_h \in [8.45, 42.25]$, $\text{Pe} \in [1, 29]$.

The influence of wall temperature, which was chosen as the characteristic fluid temperature, was also investigated. Therefore, T_w was varied between 20 and 100 °C and three different values were again considered for the nondimensional heating source, $Q = 10^{-1}$, 10^{-2}, and 10^{-3}. The channel section geometry, the wall potential and the nondimensional electric field were set to $\beta = 3/4$, $\gamma = 1/2$, $\Psi_0 = 2.92$, and $\tilde{E} = 3 \times 10^2$. As the fluid properties depend on temperature, both the Prandtl number and the Reynolds number depend on the imposed T_w, as demonstrated by Figure 11b. On the other hand, a change in the absolute fluid temperature also influences the Debye–Hückel parameter. In fact, in the range investigated, 20–100 °C, a deviation of about 13% from the reference value of $k_D D_h = 8.45$ is observed.
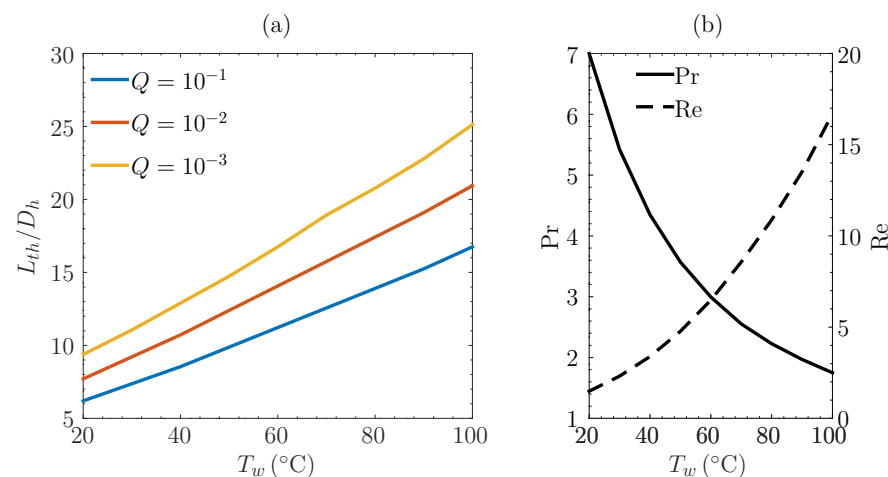

Figure 11. Thermal entry length as a function of wall temperature (**a**); variation of Prandtl and Reynolds numbers with the imposed wall temperature (**b**). $\beta = 3/4$, $\gamma = 1/2$, $\Psi_0 = 2.92$, $\tilde{E} = 3 \times 10^2$.

Figure 11a shows the dependence of the nondimensional thermal entry length on the imposed wall temperature. In accordance with $\text{Re} \, \text{Pr}$, L_{th}/D_h increases slightly nonlinearly with the imposed temperature T_w: this is readily explained if one considers that the kinematic viscosity in the expressions of the Prandtl and Reynolds numbers cancel out.

5. Conclusions

Although not the main focus of the paper, the fully developed EOF under uniform wall temperature was first investigated for channels with sharp and smoothed corners and rectangular cross sections, after validation with two different experimental works and verification with analytical and numerical cases. The numerical findings highlighted that smoothing increases both the Poiseuille and Nusselt numbers, i.e., friction and heat transfer, respectively. Two correlations which capture simultaneously the influence of the nondimensional aspect ratio β and radius of curvature γ on Po and Nu were obtained. These are recommended for design purposes, when the flow can be considered as fully developed for most of the channel length. It was also highlighted that neither the magnitude of $\tilde{E}$ (nondimensional electric field) nor Q (nondimensional Joule heating) influence the form of the velocity and temperature profiles. Similar results have not been previously reported in the literature, to the best of the Authors' knowledge.

The Graetz problem under T boundary condition was then investigated, using input parameters representative of practical applications, such as micropumps and micro heat sinks. This subject is even less explored, owing to the experimental difficulties in obtaining temperature distribution in the fluid and at the walls of the channels. Numerical studies also appear to be limited to fully-developed cases and very few are concerned with channels with smoothed corners. The investigation highlighted that high values of Q cause a reversal in the direction of the heat flux, which renders the channel unfit for its purpose. An estimate of the usable channel length under such circumstances was also provided via the solution of the temperature field over the thermal entry region under different operating conditions.

It was then demonstrated that smoothing the corners shortens L_{th}, which may significantly reduce the usable length of the channel as well, but the Nusselt number in the entry region increases with the radius of curvature. It can therefore be concluded that, when Q is sufficiently low that no heat flux reversal occurs in the channel, smoothing the corners increases the Nusselt number (for the cases investigated an improvement up to around 18% was achieved).

Finally, the thermal entry length was analyzed for different values of the model input parameters. The magnitude of the heat source term and of the variation in hydraulic diameter were investigated, with a wide range of operating conditions covered, and it was found that the nondimensional thermal entry length decreases linearly with the logarithm of Q, while scaling linearly to D_h. The dependence of L_{th} on the Reynolds and Prandtl numbers was also studied. If the Prandtl number is constant, the thermal entry length is proportional to the Reynolds number; when both vary because of changes in the reference temperature, L_{th} slightly deviates from proportionality to Re Pr because of the dependence of thermal diffusivity on temperature, whereas the kinematic viscosity cancels out.

The results presented are crucial for the design of microchannel heat sinks working with an electro-osmotic flow; moreover, knowledge of the Poiseuille number and Nusselt number over the channel length under different operating conditions is required in order to determine, e.g., the best microchannel configuration via a combined first- and second-law-based optimization under typical PEC constraints [40,43,53,54]. In the next future the Authors plan to investigate different geometries, defined by the aspect ratio β and the smoothing radius γ, and the optimal configuration determined for different PECs and different operating conditions (hydraulic diameter D_h, electric double layer thickness $k_D{}^{-1}$, electric potential E_x, source heat power Q, and Stern potential ζ). Moreover, the effect of axial conduction through the fluid can eventually be accounted for in the numerical model, in order to properly investigate electro-osmotic flows characterized by lower Reynolds numbers and, thus, lower Peclet numbers.

Nomenclature

c_p	Specific heat capacity at constant pressure	J·kg^{-1}·K^{-1}
D_0	Reference hydraulic diameter	m
D_h	Hydraulic diameter	m
e	Unit electron charge	C
E	Electric field component	V·m^{-1}
E	Electric field	V·m^{-1}
$\tilde{E}$	Nondimensional electric field	-
j	Current density vector	A·m^{-2}
k_B	Boltzmann Constant	J·K^{-1}
k_D	Debye–Hückel parameter	m^{-1}
l_c	Grid spacing parameter	-
L	Channel length	m
L_{th}	Thermal entry length	m
L_0	Adiabatic channel length	m
N_p	Number of nodes	-
N_t	Number of triangular elements	-
Nu	Nusselt number	-
Pe	Peclet number	-
Pr	Prandtl number	-
q'''	Joule heating	W·m^{-3}
Q	Quantity defined by Equation (A11)	-
R	Nondimensional radial coordinate	-
Re	Reynolds number	-
T	Temperature	K
u	Velocity component along the x-axis	m·s^{-1}
u	Velocity vector	m·s^{-1}
U	Nondimensional velocity	-
x	Axial coordinate	m
X	Nondimensional coordinate vector	-
X	Nondimensional x-coordinate	-
Y	Nondimensional y-coordinate	-
z_i	Ion valence	-
Z	Nondimensional z-coordinate	-
Greek letters		
β	Aspect ratio of the channel	-
γ	Nondimensional smoothing radius	-
Γ	Cross-sectional heated perimeter (nondimensional)	-
$\partial\Omega$	Nondimensional perimeter	-
ϵ	Absolute permittivity	F·m^{-1}
λ	thermal conductivity	W·m^{-1}·K^{-1}
μ	fluid viscosity	Pa·s^{-1}
μ_{eo}	Mobility factor	m^2·V^{-1}·s^{-1}
Ω	Nondimensional cross-sectional area	-
P	Power	W
ψ	electric potential	V
Ψ	nondimensional electric potential	-
Ψ_0	nondimensional Stern potential	-
ρ	Fluid density	kg·m^{-3}

ρ_e	electric charge density	C·m^{-2}
σ	electric conductivity	S·m^{-1}
Θ	Nondimensional temperature	K
ζ	Stern potential	V
Subscripts		
b	Bulk	
i	Inlet	
th	Thermal	
w	Wall	
x	Component along the x-direction	
∞	Fully developed	

Appendix A

This appendix reports the governing equations for the electric potential, velocity, and temperature fields of EOF (i.e., motion of polar fluids through sub-millimeter channels when electric fields are applied across the duct), and the quantities that are introduced to obtain the nondimensional forms reported in Section 2. The interested reader is also referred to the book by Kirby [24], for an extensive treatment of the phenomenon, with the books by Tabeling and Bruus [25,55] offering a more succinct overview. For the purpose of this work, the portion of fluid close to the wall where charge density is non-uniform is treated with the Gouy–Chapman model, in which a net charge at the walls, due to adsorption and ionization, balances a mobile, diffuse charge density; the two regions constitute the electric double layer (EDL), with the potential at the separation plane, the so-called Stern potential, ζ, used as a boundary condition, see in [45] for further details.

Appendix A.1. Electric Potential Field

The governing equation for the electric potential field can be derived from the Maxwell equation, which relates the electric charge distribution ρ_e to the resulting electric field **E**,

$$\nabla \cdot \mathbf{E} = \frac{\rho_e}{\epsilon} \tag{A1}$$

where ϵ is the absolute permittivity of the fluid. Following the work in [45], the electric potential can be analytically obtained from its balance equation,

$$\rho_e = 2 \, z_i \, e \, c_0 \sinh\left(\frac{z_i \, e}{k_B \, T} \psi \right) \tag{A2}$$

where $e = 1.6021 \times 10^{-19}$ (C) is the unit electron charge, $k_B = 1.3805 \times 10^{-23}$ (J/K) is the Boltzmann constant, z_i is the valence of an ion, T is the thermodynamic temperature, and ψ is the electric potential.

Thus, substituting the charge density ρ_e to Equation (A1) and using the definition of the potential of an electric field, $\mathbf{E} = -\nabla \psi$, gives the governing Poisson–Boltzmann equation,

$$\nabla^2 \psi = \frac{2 \, z_i \, e \, c_0}{\epsilon} \sinh\left(\frac{z_i \, e}{k_B \, T} \psi \right) \tag{A3}$$

which must be solved in order to find the unknown electric potential ψ. Introducing the following nondimensional quantities,

$$\mathbf{X} = \frac{\mathbf{x}}{D_h}, \ \Psi = \frac{z_i \, e}{k_B \, T} \psi \tag{A4}$$

and further assuming that $\partial\Psi/\partial X \ll \partial\Psi/\partial Y, \ \partial\Psi/\partial Z$ (i.e., electric potential does not change along channel axis), Equation (A3) becomes Equation (1).

Appendix A.2. Velocity Field

The velocity profile is computed for the conditions stated in Section 2.2. Further, neglecting the pressure gradient along the flow direction and assuming that the only body force acting on the fluid is given by the electric field along the channel axis, $\mathbf{E} = E_x\,\hat{\mathbf{i}}$, the momentum transport equation gives [45]

$$\mu \nabla^2 \mathbf{u} + \rho_e \mathbf{E} = 0 \tag{A5}$$

Introducing the following quantities,

$$u_0 = \frac{2\,c_0\,e\,\zeta\,D_h}{\mu}, \; U = \frac{u}{u_0}, \; \tilde{E} = \frac{E_x\,D_h}{\zeta} \tag{A6}$$

the nondimensional form, Equation (4), is obtained.

The Poiseuille number is computed from the solution of the nondimensional velocity field, as

$$\mathrm{Po} = \frac{1}{2\,U_b\,\Omega} \int_\Omega \tilde{E} \sinh \Psi \, \mathrm{d}\Omega \tag{A7}$$

where U_b is the nondimensional bulk velocity:

$$U_b = \frac{\int_\Omega U \, \mathrm{d}\Omega}{\int_\Omega \, \mathrm{d}\Omega} \tag{A8}$$

Appendix A.3. Temperature Field

The temperature field is obtained through the solution of the energy equation. Introducing the source term q''' deriving from Joule heating due to the electrical current density flux $\mathbf{j} = \sigma\,\mathbf{E}$,

$$q''' = \mathbf{j} \cdot \mathbf{E} = \sigma\,E_x{}^2 \tag{A9}$$

σ being the electric conductivity of the fluid, the energy equation gives

$$\rho\,u\,c_p \frac{\partial T}{\partial x} = \lambda\,\nabla^2 T + \sigma\,E_x{}^2 \tag{A10}$$

Neglecting axial conduction and introducing the following nondimensional quantities,

$$\Theta = \frac{T - T_w}{T_w - T_i}, \; Q = \frac{\sigma\,(D_h\,E_x)^2}{\lambda\,(T_w - T_i)} \tag{A11}$$

with T_i and T_w the prescribed inlet temperature and the wall temperature, respectively, Equation (A10) is made nondimensional. From its solution, the Nusselt number, Nu, can be computed as

$$\mathrm{Nu}(X) = -\frac{\int_{\partial\Omega} \nabla\Theta|_X \cdot \hat{\mathbf{n}} \, \mathrm{d}\Gamma}{\Gamma\,\Theta_b(X)} \tag{A12}$$

where $\Gamma = \partial\Omega$ is the cross-sectional heated perimeter, $\hat{\mathbf{n}}$ is the outward normal direction to $\partial\Omega$, and Θ_b is the bulk temperature:

$$\Theta_b(X) = \frac{\int_\Omega U\,\Theta|_X \, \mathrm{d}\Omega}{\int_\Omega U \, \mathrm{d}\Omega} \tag{A13}$$

After the fully developed flow condition is reached, which means $\Theta(X, Y, Z) \sim \Theta_\infty(Y, Z)$ under T-boundary condition, the fully developed Nusselt number can be computed as

$$\mathrm{Nu}_\infty = \frac{Q\,\Omega}{\Gamma\,\Theta_b|_{X\to\infty}} \tag{A14}$$

Note that the developed temperature field $\Theta_\infty(Y, Z)$ can be either estimated as $\Theta(X, Y, Z)|_{X \to \infty}$ or via the solution over the 2D channel cross section of the following partial differential equation,

$$\frac{\partial^2 \Theta}{\partial Y^2} + \frac{\partial^2 \Theta}{\partial Z^2} + Q = 0 \tag{A15}$$

which Equation (5) reduces to for $X \to \infty$.

References

1. Tuckerman, D.; Pease, R. High-Performance Heat Sinking for VLSI. *IEEE Electron. Device Lett.* **1981**, *2*, 126–129. [CrossRef]
2. Schubert, K.; Brandner, J.; Fichtner, M.; Linder, G.; Schygulla, U.; Wenka, A. Microstructure devices for applications in thermal and chemical process engineering. *Microscale Thermophys. Eng.* **2001**, *5*, 17–39.
3. Rostami, A.; Mujumdar, A.; Saniei, N. Flow and heat transfer for gas flowing in microchannels: A review. *Heat Mass Transf. Stoffuebertragung* **2002**, *38*, 359–367. [CrossRef]
4. Venkatesan, S.; Jerald, J.; Asokan, P.; Prabakaran, R. A Comprehensive Review on Microfluidics Technology and its Applications. *Lect. Notes Mech. Eng.* **2020**, 235–245.
5. Gilmore, N.; Timchenko, V.; Menictas, C. Microchannel cooling of concentrator photovoltaics: A review. *Renew. Sustain. Energy Rev.* **2018**, *90*, 1041–1059. [CrossRef]
6. Hossan, M.; Dutta, D.; Islam, N.; Dutta, P. Review: Electric field driven pumping in microfluidic device. *Electrophoresis* **2018**, *39*, 702–731. [CrossRef]
7. Tuckerman, D.; Pease, R.; Guo, Z.; Hu, J.; Yildirim, O.; Deane, G.; Wood, L. Microchannel heat transfer: Early history, commercial applications, and emerging opportunities. In Proceedings of the ASME 2011 9th International Conference on Nanochannels, Microchannels, and Minichannels, Edmonton, AB, Canada, 19–22 June 2011; Volume 2, pp. 739–756.
8. Kuznetsov, V. Fundamental Issues Related to Flow Boiling and Two-Phase Flow Patterns in Microchannels–Experimental Challenges and Opportunities. *Heat Transf. Eng.* **2019**, *40*, 711–724. [CrossRef]
9. Morini, G.L.; Lorenzini, M.; Colin, S.; Geoffroy, S. Experimental investigation of the compressibility effects on the friction factor of gas flows in microtubes. In Proceedings of the 4th International Conference on Nanochannels, Microchannels and Minichannels, ICNMM2006, Limerick, Ireland, 19–21 June 2006; Volume 47608, pp. 411–418.
10. Cavazzuti, M.; Corticelli, M.; Karayiannis, T. Compressible Fanno flows in micro-channels: An enhanced quasi-2D numerical model for laminar flows. *Therm. Sci. Eng. Prog.* **2019**, *10*, 10–26. [CrossRef]
11. Cavazzuti, M.; Corticelli, M.; Karayiannis, T. Compressible Fanno flows in micro-channels: An enhanced quasi-2D numerical model for turbulent flows. *Int. Commun. Heat Mass Transf.* **2020**, *111*. [CrossRef]
12. Morini, G.; Yang, Y.; Lorenzini, M. Experimental analysis of gas micro-convection through commercial microtubes. *Exp. Heat Transf.* **2012**, *25*, 151–171. [CrossRef]
13. Cavazzuti, M.; Corticelli, M. Numerical modelling of Fanno flows in micro channels: A quasi-static application to air vents for plastic moulding. *Therm. Sci. Eng. Prog.* **2017**, *2*, 43–56. [CrossRef]
14. Yang, Y.; Chalabi, H.; Lorenzini, M.; Morini, G. The effect on the nusselt number of the nonlinear axial temperature distribution of gas flows through microtubes. *Heat Transf. Eng.* **2014**, *35*, 159–170. [CrossRef]
15. Kockmann, N.; Holvey, C.; Roberge, D. Transitional flow and related transport phenomena in complex microchannels. In Proceedings of the 7th International Conference on Nanochannels, Microchannels, and Minichannels 2009, ICNMM2009, Pohang, Korea, 22–24 June 2009; Volume 43499, pp. 1301–1312.
16. Lorenzini, M.; Daprá, I.; Scarpi, G. Heat Transfer for a Giesekus Fluid in a Rotating Concentric Annulus. *Appl. Therm. Eng.* **2017**, *122*, 118–125. [CrossRef]
17. Ohadi, M.; Choo, K.; Dessiatoun, S.; Cetegen, E.E. *Next Generation Microchannel Heat Exchangers*; Springer Briefs in Applied Sciences and Technology; Springer: New York, NY, USA; Berlin/Heidelberg, Germany, 2013.
18. Han, Y.; Liu, Y.; Li, M.; Huang, J. A review of development of micro-channel heat exchanger applied in air-conditioning system. *Energy Procedia* **2012**, *14*, 148–153. [CrossRef]
19. Kew, P.; Reay, D. Compact/micro-heat exchangers - Their role in heat pumping equipment. *Appl. Therm. Eng.* **2011**, *31*, 594–601. [CrossRef]
20. Henning, T.; Brandner, J.; Schubert, K.; Lorenzini, M.; Morini, G. Low-frequency instabilities in the operation of metallic multi-microchannel evaporators. *Heat Transf. Eng.* **2007**, *28*, 834–841. [CrossRef]
21. Keepaiboon, C.; Dalkilic, A.; Mahian, O.; Ahn, H.; Wongwises, S.; Mondal, P.; Shadloo, M. Two-phase flow boiling in a microfluidic channel at high mass flux. *Phys. Fluids* **2020**, *32*. [CrossRef]
22. Wei, T.W.; Oprins, H.; Fang, L.; Cherman, V.; De Wolf, I.; Beyne, E.; Baelmans, M. Nozzle scaling effects for the thermohydraulic performance of microjet impingement cooling with distributed returns. *Appl. Therm. Eng.* **2020**, *180*. [CrossRef]
23. Morini, G.; Spiga, M. The role of the viscous dissipation in heated microchannels. *J. Heat Transf.* **2007**, *129*, 308–318. [CrossRef]
24. Kirby, B. *Micro- and Nanoscale Fluid Mechanics*; Cambridge University Press: Cambridge, UK, 2010.
25. Bruus, H. *Theoretical Microfluidics*; OUP: Oxford, UK, 2010.

26. Al-Rjoub, M.F.; Roy, A.K.; Ganguli, S.; Banerjee, R.K. Assessment of an active-cooling micro-channel heat sink device, using electro-osmotic flow. *Int. J. Heat Mass Transf.* **2011**, *54*, 4560–4569. [CrossRef]
27. Rice, C.; Whitehead, R. Electrokinetic flow in a narrow cylindrical capillary. *J. Phys. Chem.* **1965**, *69*, 4017–4024. [CrossRef]
28. Mala, G.; Li, D.; Werner, C.; Jacobasch, H.J.; Ning, Y. Flow characteristics of water through a microchannel between two parallel plates with electrokinetic effects. *Int. J. Heat Fluid Flow* **1997**, *18*, 489–496. [CrossRef]
29. Wang, C.Y.; Chang, C.C. Electro-osmotic flow in polygonal ducts. *Electrophoresis* **2011**, *32*, 1268–1272. [CrossRef]
30. Vocale, P.; Geri, M.; Cattani, L.; Morini, G.; Spiga, M. Electro-osmotic heat transfer in elliptical microchannels under H1 boundary condition. *Int. J. Therm. Sci.* **2013**, *72*, 92–101. [CrossRef]
31. Vocale, P.; Geri, M.; Morini, G.; Spiga, M. Electro-osmotic flows inside triangular microchannels. *J. Phys. Conf. Ser.* **2014**, *501*, 012026. [CrossRef]
32. Geri, M.; Lorenzini, M.; Morini, G. Effects of the Channel Geometry and of the Fluid Composition on the Performance of DC Electro-osmotic Pumps. *Int. J. Therm. Sci.* **2012**, *55*, 114–121. [CrossRef]
33. Morini, G.L.; Lorenzini, M.; Salvigni, S.; Spiga, M. Thermal performance of silicon micro heat-sinks with electrokinetically-driven flows. In Proceedings of the 3rd International Conference on Microchannels and Minichannels, Toronto, ON, Canada, 13–15 June 2005; Volume B, pp. 231–236.
34. Al-Rjoub, M.; Roy, A.; Ganguli, S.; Banerjee, R. Enhanced electro-osmotic flow pump for micro-scale heat exchangers. In Proceedings of the ASME 2012 3rd International Conference on Micro/Nanoscale Heat and Mass Transfer, MNHMT 2012, Atlanta, GA, USA, 3–6 March 2012; pp. 829–833.
35. Pramod, K.; Sen, A. Flow and heat transfer analysis of an electro-osmotic flow micropump for chip cooling. *J. Electron. Packag. Trans. ASME* **2014**, *136*, 03101201–03201214. [CrossRef]
36. Shamshiri, M.; Khazaeli, R.; Ashrafizaadeh, M.; Mortazavi, S. Electroviscous and thermal effects on non-Newtonian liquid flows through microchannels. *J. Non-Newton. Fluid Mech.* **2012**, *173–174*, 1–12. [CrossRef]
37. Shit, G.; Mondal, A.; Sinha, A.; Kundu, P. Electro-osmotic flow of power-law fluid and heat transfer in a micro-channel with effects of Joule heating and thermal radiation. *Phys. A Stat. Mech. Its Appl.* **2016**, *462*, 1040–1057. [CrossRef]
38. Al-Rjoub, M.; Roy, A.; Ganguli, S.; Banerjee, R. Enhanced heat transfer in a micro-scale heat exchanger using nano-particle laden electro-osmotic flow. *Int. Commun. Heat Mass Transf.* **2015**, *68*, 228–235. [CrossRef]
39. Ray, S.; Misra, D. Laminar fully developed flow through square and equilateral triangular ducts with rounded corners subjected to H1 and H2 boundary conditions. *Int. J. Therm. Sci.* **2010**, *49*, 1763–1775. [CrossRef]
40. Chakraborty, S.; Ray, S. Performance optimisation of laminar fully developed flow through square ducts with rounded corners. *Int. J. Therm. Sci.* **2011**, *50*, 2522–2535. [CrossRef]
41. Lorenzini, M.; Morini, G. Single-phase, Laminar Forced Convection in Microchannels with Rounded Corners. *Heat Transf. Eng.* **2011**, *32*, 1108–1116. [CrossRef]
42. Lorenzini, M. The Influence of Viscous Dissipation on Thermal Performance of Microchannels with Rounded Corners. *La Houille Blanche* **2013**, 64–71. [CrossRef]
43. Lorenzini, M.; Suzzi, N. The influence of geometry on the thermal performance of microchannels in laminar flow with viscous dissipation. *Heat Trans. Eng.* **2016**, *37*, 1096–1104. [CrossRef]
44. Lorenzini, M. Electro-osmotic Flow in Rectangular Microchannels: Geometry Optimisation. *J. Phys. Conf. Ser.* **2017**, *923*, 1–8. [CrossRef]
45. Lorenzini, M. Electro-osmotic non-isothermal flow in rectangular channels with smoothed corners. *J. Therm. Sci. Eng. Appl.* **2020**, *19*, 100617.
46. Webb, R. *Principles of Enhanced Heat Transfer*; Wiley: New York, NY, USA, 1984.
47. Shah, R.K.; London, A.K. *Laminar Flow Forced Convection in Ducts—A Source Book for Heat Exchanger Analytical Data*; Academic Press: New York, NY, USA, 1978.
48. Barletta, A.; Magyari, E. The Graetz-Brinkman problem in a plane-parallel channel with adiabatic-to-isothermal entrance. *Int. Commun. Heat Mass* **2006**, *33*, 677–685. [CrossRef]
49. Suzzi, N.; Lorenzini, M. Viscous heating of a laminar flow in the thermal entrance region of a rectangular channel with rounded corners and uniform wall temperature. *Int. J. Therm. Sci.* **2019**, *145*, 106032. [CrossRef]
50. Morini, G.L.; Lorenzini, M.; Salvigni, S.; Spiga, M. Thermal performance of silicon micro heat-sinks with electrokinetically-driven flows. *Int. J. Therm. Sci.* **2006**, *45*, 955–961. [CrossRef]
51. Jian, Y.; Yang, L.; Liu, Q. Time periodic electro-osmotic flow through amicroannulus. *Phys. Fluids* **2010**, *22*, 042001. [CrossRef]
52. Sadr, R.; Yoda, M.; Zheng, Z.; Conlisk, T. An experimental study of electro-osmotic flow in rectangular microchannels. *J. Fluid Mech.* **2004**, *506*, 357–367. [CrossRef]
53. Zimparov, V. Extended performance evaluation criteria for enhanced heat transfer surfaces: Heat transfer through ducts with constant wall temperature. *Int. J. Heat Mass Transf.* **2000**, *43*, 3137–3155. [CrossRef]
54. Zimparov, V. Extended performance evaluation criteria for enhanced heat transfer surfaces: Heat transfer through ducts with constant heat flux. *Int. J. Heat Mass Transf.* **2001**, *44*, 169–180. [CrossRef]
55. Tabeling, P. *Introduction to Microfluidics*; Oxford University Press: Oxford, UK, 2010.